Appendix

Geophysical constraints on the magma ascent processes of the 2011 Shinmoedake eruption

Based on precise geodetic observations of volcanic edifice deflation with tilt meters and synthetic aperture radar (SAR) and of weather radar observations of the eruption cloud heights, the deflation of the magma chamber was detected synchronously at the formation time of the eruption column. This reveals that the sub-Plinian eruptions and lava extrusion were accompanied by simultaneous and continuous magma supplied from the magma chamber through an open conduit with direct connection to the surface. The following lava effusion that began 36 h after the last sub-Plinian eruption was also accompanied by deflation of the magma chamber. However, the Vulcanian explosions were not accompanied by magma chamber deflation, which indicates that the eruption was caused by the rupture of a pressurized shallow conduit and was not followed by magma migration from the chamber (Kozono et al., 2013; Kozono et al., 2014). The erupted volume and discharge rate during the sub-Plinian eruptions and lava extrusion were estimated to be 3.04–6.67 × 10^6 m^3 and 450–741 m^3/s and 12.1–15.1 × 10^6 m^3 and 70.0–87.4 m^3/s, respectively (Kozono et al., 2013). It should be noted that these discharge rates are within one order of magnitude, although the mode of eruption is quite different. This is consistent with the observation of the eruption changing from sub-Plinian eruption to lava effusion without a long pause. Assuming the conduit radius is 5 m (Sato et al., 2013), the magma ascent rate for the sub-Plinian eruptions was calculated to be 5.7–9.4 m/s, whereas that for the lava extrusion was 0.89–1.1 m/s; the latter is one fifth to one ninth of the former. Based on the one-dimensional steady flow model, Tanaka and Hashimoto (2013) estimated the magma fragmentation pressure to be about 10 MPa.

Semi-log CSD plots and the 2D raw data

Here we used CSDCorrections version 1.54 (Higgins, 2000) to convert 2D measurements of the short axis of the best-fitting box to 3D crystal size distributions on a vesicle-free basis. Utilizing CSDCorrections requires estimation of the sample fabric and grain roundness, in addition to the 3D crystal shape. Samples were assumed to be free of fabric. Based on visual inspection of the samples, a roundness factor of 0.4 for pyroxene and 0.2 for plagioclase were chosen. The 3D shapes of crystals were determined using CSDSlice version 5 (Morgan and Jerram, 2006). The 3D crystal shapes of pyroxene were mostly acicular (1.0:1.0–2.3:7.0–10) and that of all plagioclase were rectangular prisms (1.0:3.4–5.0:10). The 2D raw data obtained separately from W-SEM (low magnification; LM) and FE-SEM (high magnification; HM) were loaded to CSDCorrections to produce single line. In order to compare the data among different eruption styles, we used a common crystal shapes of 1:1:8 for pyroxene and 1:5:10 for plagioclase, respectively, and number of bin/decade of 5 for both minerals.

Semi-log CSD plots from 0.1 μm to 5.2 μm in width shown in Figure S2 are the revised versions of those reported by Mujin and Nakamura (2014) using the simple method of Wager (1961). It should be noted that Wager (1961)'s conversion method does not have a good theoretical basis and does not give accurate results (Higgins, 2000). The raw data are the same as those in Mujin and Nakamura (2014) and these are shown in the crystal width frequency histograms (Fig. S1). Here, we obtained the crystal number density (N) with the following equation:

$$N \text{ (in m}^{-4}) = (\text{number of crystals per analyzed area})^{1.5}/\text{length interval} \quad (1)$$

In the preceding paper, the value was calculated by (number of crystals per analyzed area/length interval)$^{1.5}$, which gave higher N values in $m^{-4.5}$. The length interval was set at 300 nm in all calculations, which enabled comparison of the CSD plots in this paper. As found previously, the CSD plots of pyroxene and plagioclase exhibited a kink at crystal widths of 2.0–2.7 μm for all erupted materials except for the plagioclase in the sub-Plinian pumices. The plagioclase in the sub-Plinian pumices produced an almost constant CSD slope down to a size of 400 nm. The semi-log CSDs parameters (the values of intercept, $\ln N_0$, and slope -1/a) are shown in Table S1.

References cited

Higgins, M.D. (2000) Measurement of crystal size distributions. American Mineralogist, 85, 1105–1116.

Kozono, T., Ueda, H., Shinmbori, T., and Fukui, K. (2014) Correlation between magma chamber deflation and eruption cloud height during the 2011 Shinmoedake eruptions. Earth, Planets and Space, 66, 139–147.

Kozono, T., Ueda, H., Ozawa, T., Koyaguchi, T., Fujita, E., Tomiya, A., and Suzuki, Y.J. (2013) Magma discharge variations during the 2011 eruptions of Shinmoedake volcano, Japan, revealed by geodetic and satellite observations. Bulletin of Volcanology, 75, 695–707.

Morgan, D.J., and Jerram, D.A. (2006) On estimating crystal shape for crystal size distribution analysis. Journal of Volcanology and Geothermal Research, 154, 1–7.

Mujin, M., and Nakamura, M. (2014) A nanolite record of eruption style transion. Geology, 42, 661–614.

Sato, H., Suzuki-Kamata, K., Sato, E., Sano, K., Wada, K., and Imura, R. (2013) Viscosity of andesitic lava and its implications for possible drain-back processes in the 2011 eruption of Shinmoedake volcano, Japan. Earth Planets Space, 65, 623–631.

Tanaka, R., and Hashimoto, T. (2013) Transition in eruption style during the 2011 eruption of Shinmoe-dake, in the Kirishima volcanic group: Implications from a steady conduit flow model. Earth, Planets and Space, 65, 645–655.

Wager, L.R. (1961) A note on the origin of ophitic texture in the chilled olivine gabbro of the Skaergaard intrusion. Geological Magazine, 98, 353–364.

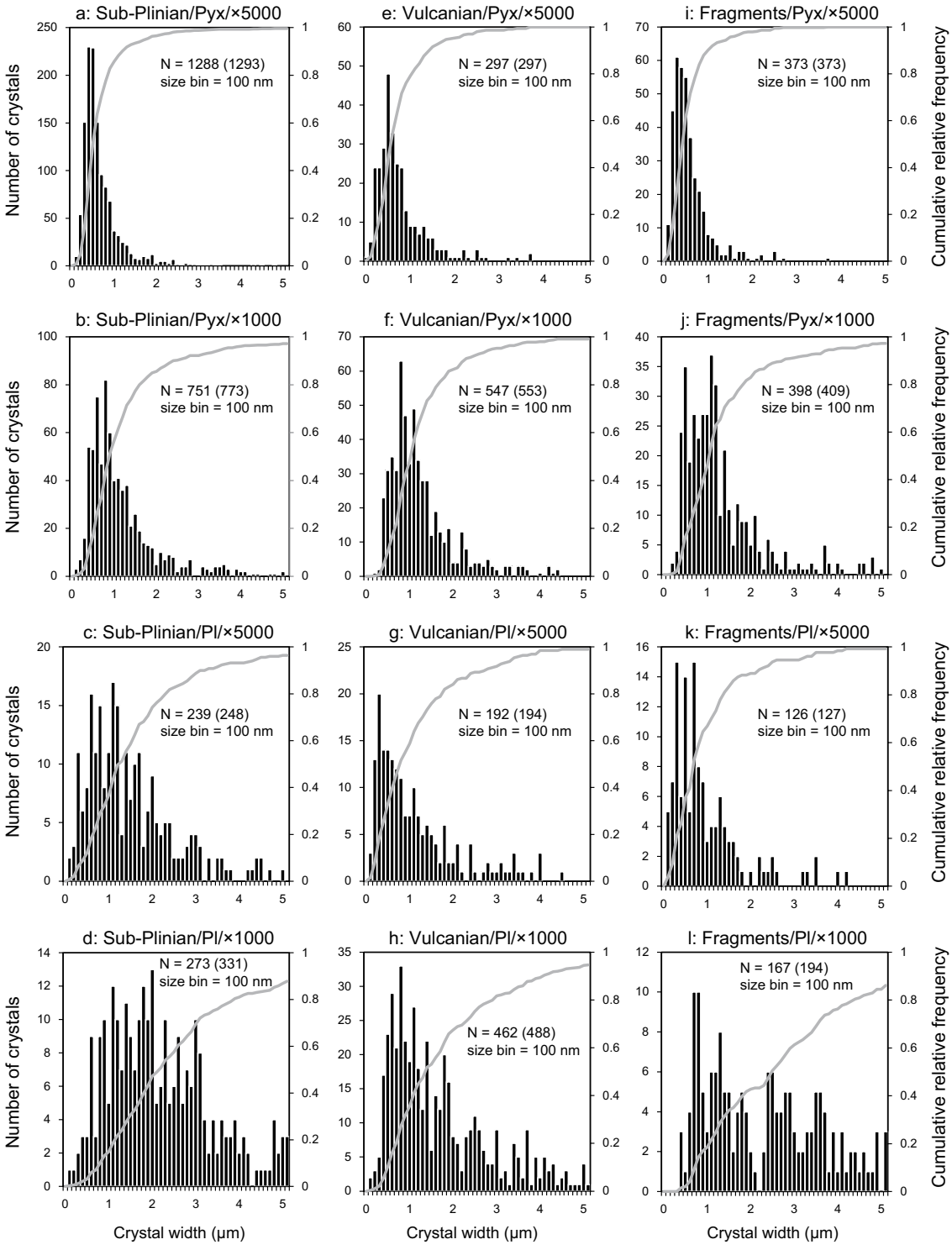

FIGURE S1. Frequency histograms of crystal width in the size range of 0.1–5.2 μm for sub-Plinian pumices **(a–d)**, Vulcanian pumices **(e–h)**, and dense juvenile fragments **(i–l)**, obtained from back-scattered electron images taken with a field emission scanning electron microscope (FE-SEM) at a magnification of ×5000 **(a, c, e, g, i, and k)** and with an SEM with a tungsten filament (W-SEM) at a magnification of ×1000 **(b, d, f, h, j, and l)**. Each panel includes the total number of crystals measured in the size range of 0.1–5.2 μm and the size bin. Figures in parentheses are the total number of crystals including those larger than 5.2 μm. Cumulative relative frequency is shown in each panel.

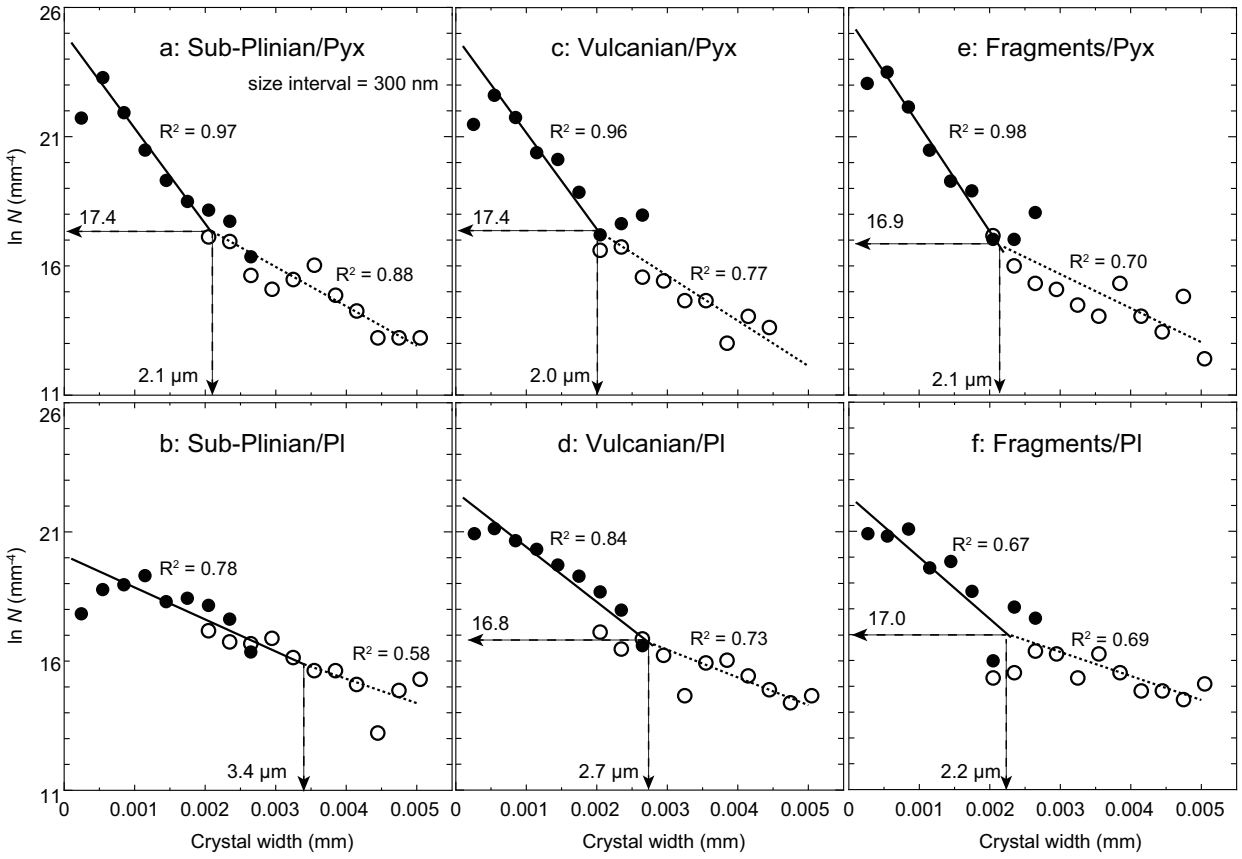

FIGURE S2. Semi-log crystal size distribution (CSD) plots for pyroxene (Pyx; upper row) and plagioclase (Pl; lower row) in the size range of 0.1–5.2 μm. Here, the number densities per unit volume (N m^{-4}) were obtained by raising the number of crystals per unit area to the 3/2 power and dividing it by the size interval. The size interval is 300 nm for all panels. **(a) and (b)**: pumices of the sub-Plinian eruptions; **(c) and (d)**: pumices of the Vulcanian explosions; **(e) and (f)**: dense juvenile fragments of the Vulcanian explosions. The data were fitted with two straight lines, which are shown by solid and dotted lines with the least error sum of squares (R^2). The width and N at the junction of the two fitting lines are shown. Open and solid circles represent data obtained using scanning electron microscopy with a tungsten filament (W-SEM) and field emission (FE-SEM), respectively.

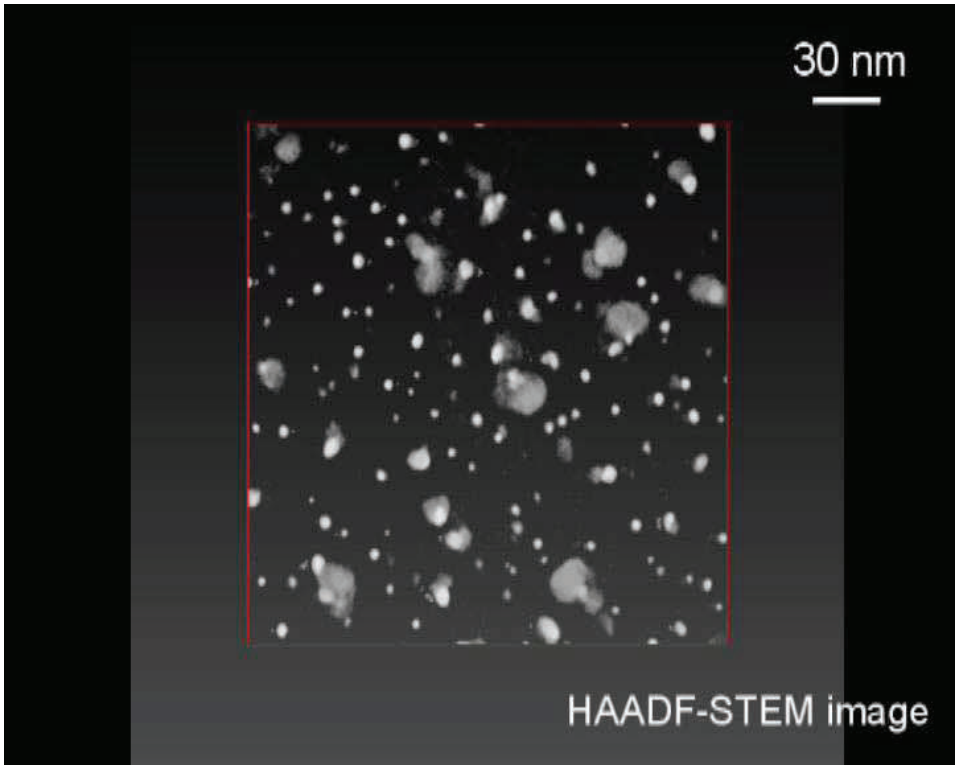

SUPPLEMENTAL MATERIAL 1. *Still frame.* Transmission electron microtomography (TEMT) of high-angle annular dark-field scanning transmission electron microscopy (HAADF-STEM) of pyroxenes (lower brightness) and possibly Fe–Ti oxide (higher brightness) in a dense juvenile fragment showing homogeneous nucleation of Fe–Ti oxide ultrananolites. (See additional files for the video.)